Forward modeling of radio imaging (RIM) data with the Comsol RF module

Yongxing Li *, Richard S. Smith

Laurentian University, 935 Ramsey Lake Road, Sudbury, Ontario, Canada, P3E 2C6

ABSTRACT

Radio imaging method (RIM) is an electromagnetic (EM) tomographic method, which can be applied to image the electrical properties (principally the conductivity) in the plane defined by two boreholes. RIM employs the EM waves at radio frequencies between 100 kHz and 10 MHz, and the manner that these waves propagate around subsurface ore bodies has not been studied thoroughly. We studied the wave propagation using the finite element modeling (FEM) algorithm as implemented in the Comsol RF module. An appropriate element size is quantified by comparing the Comsol modeling results of 6 types of element sizes at 4 frequencies with the analytical solution in the homogeneous whole space. The FEM model data with 5 elements per wavelength have errors less than 5%; 7–8 elements per wavelength provide the errors around 1%; when there are 10 elements per wavelength, the errors are less than 1%. Comparison studies for more complicated models with anomalous conductivity structures show that the Comsol modeling results are consistent with results derived from analytical solutions, finite-difference time-domain methods and integral equations. To illustrate the flexibility of the Comsol method for RIM modeling, we provide an example with two moderately conductive bodies between boreholes. Receiver profiles and a relative variation map show that when the conductive bodies are two wavelengths away from the source, the EM wave attenuation and reflection by the conductive bodies can be observed. The amplitude tomography of the model data reveals that with the SIRT algorithm, the location of the conductive anomalies can be reconstructed successfully, although, some limitations exist such as low resolution, incorrect conductivity estimation, and some artifacts. From our work, we conclude that Comsol modeling is helpful to study radio wave propagation and imaging methods.

© 2015 Elsevier Ltd. All rights reserved.

1. Introduction

The radio imaging method (RIM), also known as radio-frequency tomography, is a cross-hole geophysical method, which employs radio-frequency electromagnetic (EM) waves to image the distribution of electric properties between boreholes. RIM can be applied to prediction of coal-seam hazards (Hill, 1984), delineation of ore bodies (Thomson and Hinde, 1993; Zhou et al., 1998; Mutton, 2000) and site selection for underground disposal of nuclear waste (Korpisalo and Heikkinen, 2014). As shown in Fig. 1, in a RIM survey, we put a transmitter in one borehole (BH_1), and a receiver in another borehole (BH_2) and move each to a multiplicity of positions where the EM field is measured. If there is material between the boreholes that is more conductive than the background, the EM fields attenuate faster and travel more slowly. This situation results in a measured response (dotted line on the

right of Fig. 1) which is less than the response of the background only (depicted with the dashed line). In the case when the material is extremely conductive, the measured data can drop below the noise level (as depicted with the solid line on the right of Fig. 1). The situation in Fig. 1 shows the simple case of straight rays propagating directly from the transmitter to the receiver and those that strike the anomalous body being completely absorbed (attenuated). As discussed below, the situation is, in reality, more complex.

Fig. 1 shows one transmitter and a multiplicity of receivers (rays going from the transmitter to each receiver). A full tomographic survey comprises many transmitter positions at multiple depths down the hole. This full survey data is used to reconstruct an image on the cross-hole plane.

The mathematical foundation of image reconstruction is similar to X-ray computerized aided tomography (CAT) in medical imaging (Jackson and Tweeton, 1994). The idea of tomography has been successfully applied to explore the earth, with seismic waves (Dines and Lytle, 1979) or high-frequency (typically 10–1500 MHz)
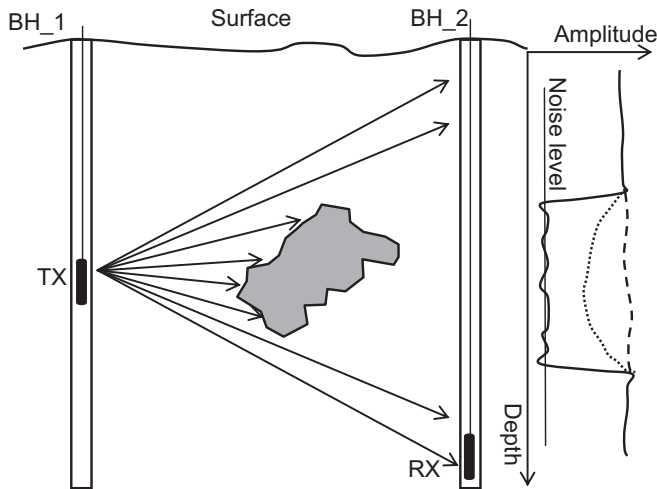
Fig. 1. Diagram of radio imaging method. This shows one transmitter (TX) position in the left hole (BH_1). The receiver is lowered down the right hole (BH_2). Three amplitude profiles are shown schematically in the right panel: the dashed line is when there is no body present between holes and the dotted and solid lines show the situation when the gray body between holes results in partial and complete attenuation of the signal.

EM waves (Holliger et al., 2001). In mining exploration, we focus more on the EM waves, because the EM data can be used to infer the electric properties of minerals and the electrical properties of ore bodies are normally strongly anomalous. However, high-frequency EM waves typically attenuate quickly in the subsurface, which results in very short propagation distances (usually meters to tens of meters). Boreholes in mining exploration are usually on the order of hundreds of meters apart. Hence, it is necessary to lower the frequency to the medium frequency range (0.1–10 MHz) in order to obtain sufficient signal. However, the EM fields in this frequency range do not behave as simply as X-rays in CAT scans (as depicted on Fig. 1). In the medium-frequency range, the waves can be refracted and reflected, and as the frequency lowers, currents can be induced in the anomalous body and reradiated. A modeling tool capable of simulating all of these situations is required to better understand the RIM method. Wilkinson (2005) argued that at the medium-frequency range, the modeling tool needs to be able to account for changes in conductivity and dielectric permittivity. Additionally, Naprstek (2014) found that magnetic permeability also had an impact on the response, although this was easily confused with the impact of changes in conductivity. Hence, it is necessary to solve the full Maxwell equations and not ignore either conductivity effects or permittivity effects. Solutions that assume propagating rays generally solve the wave equation and assume the conductivity is zero, while other solutions might solve the diffusion equation and assume the permittivity is zero. A method that solves the full Maxwell equations will allow us to better understand the RIM method and hence better utilize the data.

A number of attempts have been made to model RIM data using a variety of methods. Monaghan (2007) built scaled physical models and used a corresponding higher-frequency EM wave to quantify the EM wave propagation in coal seams. The disadvantages of the scaled models are that the effects of the model boundaries were not considered; measurements are limited on the surface of the models; and model making is expensive and time-consuming. Alternatives are numerical modeling methods. Johnson (1997) employed the finite-difference time-domain method (FDTD) to model the RIM data. He investigated the interaction of the fields from a magnetic dipole with perfect electric conductors. His modeling revealed diffraction of the EM wave, which may

result in artifacts on ray-based images. His studies were restricted to highly conductive plate-like models. Other models such as layered models, spherical models and weakly conductive bodies were not studied.

Another widely used method is the finite-element method (FEM), which is not restricted to square network discretization and enables the use of tetrahedral elements, as these are more efficient for simulating complex 3-D models (Bondeson et al., 2005). Over the last decades, numerical modeling algorithms are now being built into commercial or open-source software. Comsol Multiphysics is one of the commercial numerical modeling software packages that is based on the FEM. Comsol Multiphysics has been applied to model geophysical fields, such as gravitational, magnetic, electric and electromagnetic fields (Butler and Sinha, 2012; Park et al., 2010). In this paper, we apply the Comsol Multiphysics package and specifically the RF module to model RIM data. We began by comparing the Comsol package with the analytical solution for a whole space. This allowed us to evaluate the modeling precision and define some rules for defining the element sizes in our models. Then, we built confidence in the Comsol package by comparing the results with published results from other numerical algorithms. Finally, we showed how it is possible to generate a response from a realistic field situation and how this data can be used to better understand the propagation of EM fields and tomographic imaging methods.

2. Comsol modeling

The Comsol Multiphysics package has graphic user interfaces (GUIs), which make the implementation of the FEM much easier. Complex geophysical models can be developed in this environment with simple geometries such as blocks, spheres and cylinders and the meshes or grids required for representing the fields can be generated easily. In order to simulate the EM data in the medium frequency range, we used the RF module available for the Comsol platform, as this module solves the full Maxwell's equations. With the RF module, we can assign the necessary physical properties for the full EM solution, including conductivity, dielectric permittivity and magnetic permeability. The EM field sources can be from an electric dipole, magnetic dipole, electric current or magnetic current, etc. For comparison with the analytical solutions, we used the frequency-domain electric dipole source. The configurations of dipole source include selecting the position, orientation, dipole moment and frequency.

To simulate EM fields in unbounded models, we configured perfectly matched layers (PMLs) on the edges of the models to absorb the outgoing EM waves, with the thickness defined in accordance with the users' guide (COMSOL Multiphysics User Guide, 2012). The domains of PMLs are discretized with swept meshes, which start along the grids on the surface between the inner domain and the PMLs and then mesh along the direction perpendicular to the surface, which generates prismatic elements. The swept meshes are discretized with 5 layers by default (Fig. 2b). In the inner domains, we use free tetrahedral elements to discretize the models. The user can control the sizes of the elements in every subdomain, which is useful because we often want to use finer elements in regions that we are more interested in.

After building and meshing the models, Comsol generates the partial differential equations and solves the equations on the mesh. We choose the biconjugate gradient stabilized iterative method (BiCGStab), which is time and memory efficient for the vector field (COMSOL Multiphysics User Guide, 2012).
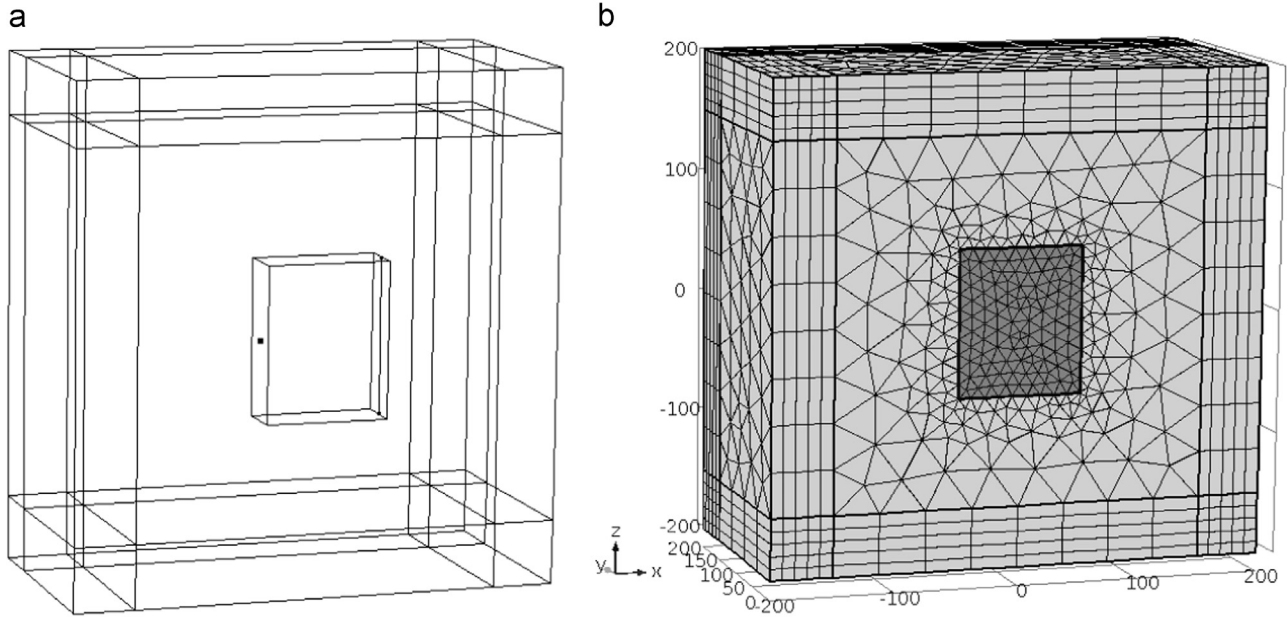
a

b

Fig. 2. (a) Transparent view of the homogeneous model without the front half. The innermost prism including the transmitter (the dot on the left) and the receiver line (the vertical line on the right) is our region of interest. (b) The region of interest (dark gray area of (b)) is meshed with Mesh Type 4. Element sizes between the region of interest and the PML can increase to 60 m. The PML is discretized with 5 layer swept meshes. (The front half is removed and the rest is meshed along the XZ-plane for illustration).

3. Tests of the Comsol software

In this section we determine the optimal element size for sampling a whole space. For non-whole-space models, we compare the Comsol results with published data of analytical solutions and other numerical methods.

3.1. Comparison with homogeneous models to determine optimal element size.

Ward and Hohmann (1988) derived the analytical solution of an electric dipole in a homogeneous whole space for low frequency EM, in which the dielectric permittivity was ignored. To calculate the EM fields in the medium frequency range, the impact of dielectric permittivity should be considered. The x-component and z-component of electric field at $P(x, y, z)$ generated by a z-directed dipole source with dipole moment Ids at the origin of Cartesian coordinates are as follow:

$$\mathbf{E_x} = \frac{I \, ds}{4\pi (\sigma + i\varepsilon\omega) r^3} \cdot \frac{xz\left(-k^2 r^2 + 3ikr + 3\right)}{r^2} e^{-ikr} \tag{1}$$

$$\mathbf{E_z} = \frac{I \, ds}{4\pi (\sigma + i\varepsilon\omega) r^3} \left[\frac{z^2\left(-k^2 r^2 + 3ikr + 3\right)}{r^2} + k^2 r^2 - ikr - 1 \right] e^{-ikr} \tag{2}$$

where, I is the transmitting current; ds is the length of the dipole; σ is the conductivity; ε is the dielectric permittivity, $\varepsilon = \varepsilon_r \cdot \varepsilon_0$, in which, ε_r is the relative permittivity and ε_0 the free space permittivity; ω is the angular frequency, $\omega = 2\pi f$, in which f is the frequency; r is the distance from the dipole to P; and k is the wave number, $k^2 = \mu\varepsilon\omega^2 - i\mu\sigma\omega$, in which, μ is the magnetic permeability, $\mu = \mu_r \cdot \mu_0$, where, μ_r is the relative permeability and μ_0 the free space permittivity. The y-component is always 0. We focus on the z-component, because, usually, only the z-component could be measured in vertical boreholes. These formulae are identical to the equation (2.40) in Ward and Hohmann (1998), except, they removed the terms with ε.

In the Comsol model building environment, we created a homogeneous model with $\sigma = 0.001$ S/m, $\varepsilon_r = 1$ and $\mu_r = 1$. The frequencies of the EM source are 312.5, 625, 1250 and 2500 kHz. These are the operating frequencies of the FARA system, which is commonly used in Sudbury, Canada. The wavelength can be calculated by the formula,

$$\lambda = \frac{2\pi}{\beta} , \tag{3}$$

where, β is the phase coefficient, which can be obtained from equation (1.48) in Ward and Hohmann (1988),

$$\beta = \left\{ \frac{\omega^2 \mu\varepsilon}{2} \left[\left(1 + \frac{\sigma^2}{\varepsilon^2 \omega^2} \right)^{1/2} + 1 \right] \right\}^{1/2} . \tag{4}$$

Using Eqs. (3) and (4), the wavelengths of these frequencies are 177, 124, 86 and 59 m respectively. The modeled region is a 400 by 400 by 400 m cube, with its center at the origin. A vertical dipole source is at $(x, y, z) = (-50, 0, 0)$, with the dipole moment 4000 Am. A 50 m-thick PML is configured on the outer surface of the region to absorb the outgoing fields. A 120 m-long receiver traverse is from $(50, 0, -60)$ to $(50, 0, 60)$. The rectangular prism that includes the source and receiver line with a strike extent of 50 m (25 m into and out of the section) is deemed our "region of interest" (as shown in Fig. 2a). In our test studies, we meshed this region with 6 types of different elements sizes, which are shown in Table 1. The first four element sizes (with maximum edge lengths of 35, 25, 17, and 12 m) are designed to meet a criterion of 5 elements per wavelength for the four frequencies (177, 124, 86 and 59 m). The Mesh Type 5 and 6 are added to study the modeling errors obtained by using even smaller element sizes. For comparison, we want the element sizes of each type to fall within a fixed range, so that adjacent mesh types do not have overlap (Table 1). From the edge of the region of interest to the PMLs, the element sizes are free to increase to as large as 60 m, which can reduce the number of elements, and hence save computation time. Fig. 2b illustrates the Mesh Type 4.

The magnitudes of the z-component model data for mesh type 2, 4 and 6 at 2.5 MHz along the receiver line are plotted in Fig. 3

Table 1
Mesh sizes and modeling error, memory usage and run time.

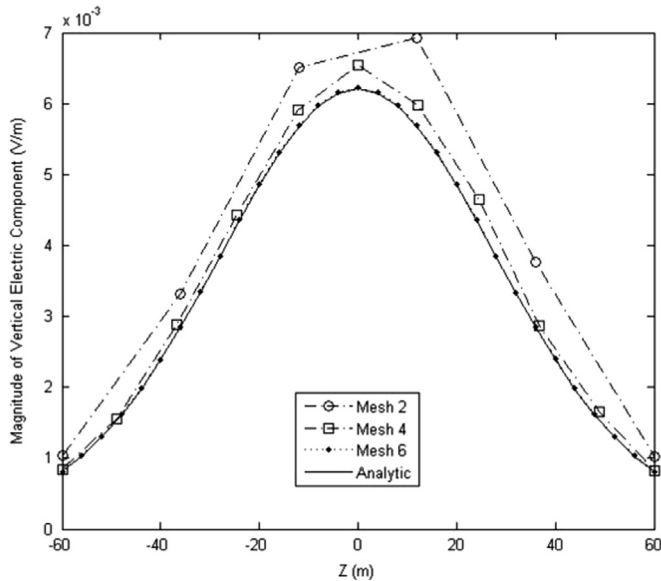| Mesh type	Element edge length	Modeling error (RMS, %)				Degrees of freedom	Memory usage (GB)	Run time (s)
		312.5 k	625 k	1.25 M	2.5 M			
1	25–35 m	**4.30**	16.40	43.00	266.87	186,084	3.11	64
2	17–25 m	*3.38*	**4.37**	7.05	23.98	188,846	3.16	66
3	12–17 m	<u>0.84</u>	0.76	**4.95**	13.28	209,284	3.26	75
4	8–12 m	0.56	<u>0.76</u>	*1.38*	**4.92**	252,842	3.53	87
5	6–8 m	0.24	0.27	<u>0.45</u>	*1.13*	373,052	4.51	130
6	3–6 m	0.10	0.17	0.24	<u>0.73</u>	574,756	5.73	186

Fig. 3. Receiver profiles of 2.5 MHz data for three different mesh sizes and the analytic solution. The mesh sizes are shown in Table 1.

with open circle, open square and solid circle symbols respectively. The figure shows that as the element size decreases, the data spacing along the receiver line decreases. The modeling errors also decrease, as smaller discrepancies between modeling data and the analytical solution (solid line) can be observed.

We calculated the Root Mean Square (RMS) of the modeling errors along the receiver line for the six mesh types at all frequencies. The results are listed in Table 1. We can see from Table 1 that the mesh types that have 5 elements per wavelength (bolded numbers) can provide a modeling precision with the errors within 5%. As the sizes become smaller to 7–8 elements per wavelength, the modeling errors converge to around 1% (italic numbers), except for the 312.5 kHz case. The reason for this is that at low frequency, the wavelength is so large that the receiver line is relatively close to the source. The near-field effect makes the EM fields more complicated. As the sizes decrease to 10 elements per wavelength, the modeling data have errors less than 1% for all four frequencies (underlined numbers).

However, greater precision comes with longer computational time and larger memory requirements. As the discretization is finer, the degrees of freedom of the partial differential equation are higher, so that it takes more time and larger memory to find a solution. The memory usage and the run times listed in Table 1 are obtained in an 8-core computer with a clock speed of 2.65 GHz. It can be observed from Table 1 that the memory usages and run times are approximately proportional to the degrees of freedom. However, the algorithm takes more time when the model is more complex. In the heterogeneous modeling example we present in the next section, the degrees of freedom is around 7 million, while

the memory usage is 86.7 GB and the run time is 4130 s (69 min) for 1 transmitter location. This run time is almost twice as large as would have been predicted from Table 1.

Therefore, to maintain reasonable modeling precision with affordable computational time and memory, we recommend element sizes smaller than or comparable to 7 elements per wavelength within the region of interest, while outside of the region of interest, the element sizes could increase to be much larger to save memory and computation time.

The optimal mesh sizes have been derived by comparison with a whole-space model. In order to gain confidence that these mesh sizes can be applied more generally, we have calculated the response using Comsol for models that have been published in the literature that contain heterogeneous bodies in a uniform background.

3.2. Comparison of Comsol and published results for anomalous models

The Comsol RF module has been compared with the analytical solutions and a FDTD numerical modeling code for a spherical model. The profiles plotted on Fig. 4 are the solutions of conductive spherical anomalies of differing conductivity in a homogeneous whole space. Two transmitters are at point A (0, 0, 2) and
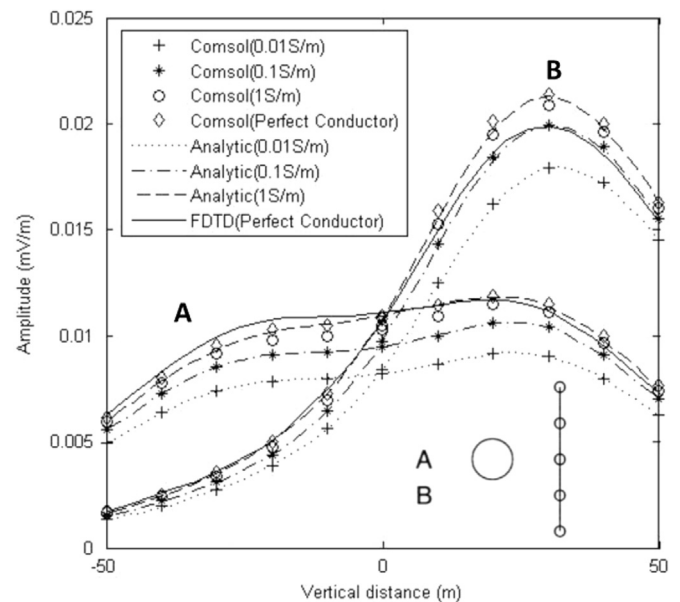

Fig. 4. Modeling results of spherical models with different conductivities calculated by Comsol Multiphysics, compared with the analytical solutions and the FDTD solution. The conductivities of the sphere and the solution methods are shown in the legend. The results derived by the analytical solution and the FDTD method are from Yu et al. (1998). The geometry is shown as a cross section view in button right of the figure and the five open circles represent the receiver locations (although there are more than 5).

Table 2
Wavelengths and element sizes for anomalous models.

Spherical model ($\varepsilon_r=3$, $\mu_r=1$)			Cubic model ($\varepsilon_r=10$, $\mu_r=1$)		
σ (S/m)	λ (m)	Max. element (m)	σ (S/m)	λ (m)	Max. element (m)
0.001	92.03	10	0.001	76.68	10
0.01	31.36	4	0.1	9.97	2
0.1	9.99	2			
1	3.16	1			
∞	$1/\infty$	1			

point B (0, 0, 22), with the transmission frequency 1 M Hz, and the dipole moment 1 Am. The center of the spherical body is at (50, 0, 0) and its radius is 20 m. The receiver line is from (100, 0, −50) to (100, 0, 50). The physical properties of the background are $\sigma=0.001$ S/m, $\varepsilon_r=3$, $\mu_r=1$. The geometry of the transmitter points, the sphere and the receiver line is shown on the bottom right of Fig. 4. All of these parameters are fixed, but the conductivities of the sphere are 0.01, 0.1, 1 S/m, and in the limit that the sphere is defined to be a perfect conductor ($\sigma\rightarrow\infty$). The wavelengths and the maximum element edge lengths in the sphere and the background are in the left of Table 2. The element sizes are designed to meet at lease the 1/5th wavelength requirement, except for 1 S/m sphere as the computation time would be too large. The perfect conductor is simulated with perfectly conductive boundary condition, so the element sizes in the sphere do not matter in this case. In Fig. 4, the analytical solutions of the spherical models with conductivity 0.01, 0.1, 1 S/m and the FDTD solution of the perfectly conductive sphere are from Yu et al. (1998). We can see that the Comsol modeling results match the analytical solutions very well, especially for models with conductivity of 0.01 and 0.1 S/m. The Comsol modeling results show the more conductive the sphere, the higher the data values, such that the largest data profile is the solution of a perfect conductor. Whereas, the FDTD profile is erratic, with some parts being too large and other parts lie between the analytical solutions of 0.1 and 1.0 S/m. Hence, we argue that for this model, the Comsol results are better than the FDTD result.

Our second test study compares the FDTD and the integral equations solutions (Xiong and Tripp, 1997) of a cubic model, also published in Yu et al. (1998). Transmitters are at slightly different location points A (0, 0, 0) and B (0, 0, 30), with the same operating frequency and dipole moment as the previous example. The size of the cube is $24\times24\times24$ m^3, with its center at (50, 0, 0). The receiver line is also the same as the previous model and the geometry is depicted on the top left Fig. 5. The relative permittivity and the relative permeability are 10 and 1 respectively for the whole model. The background conductivity is 0.001 S/m, while the conductivity of the cube is 0.1 S/m. The wavelengths and the element sizes are in the right of Table 2. In Fig. 5, the solid line shows the Comsol solution; the asterisksthe FDTD solution and the dashed-dotted line the integral equation solution. It can be seen from the figure that the Comsol solutions are comparable with the FDTD solutions and the integral equation solutions. From these two results we conclude that the guidelines we have developed for element sizes yield good results in anomalous regions.

4. Modeling example

Here we provide a demonstration that Comsol can be used to study the EM fields of more realistic scenarios. We also use the modeled data to study the efficacy of a tomographic image reconstruction method in the case when the true model is known. Fig. 6a is an XZ plane view (at $y=0$) of the 3D model. The transmitter borehole (TX) is from (0, 0, 100) to (0, 0, 440), with the
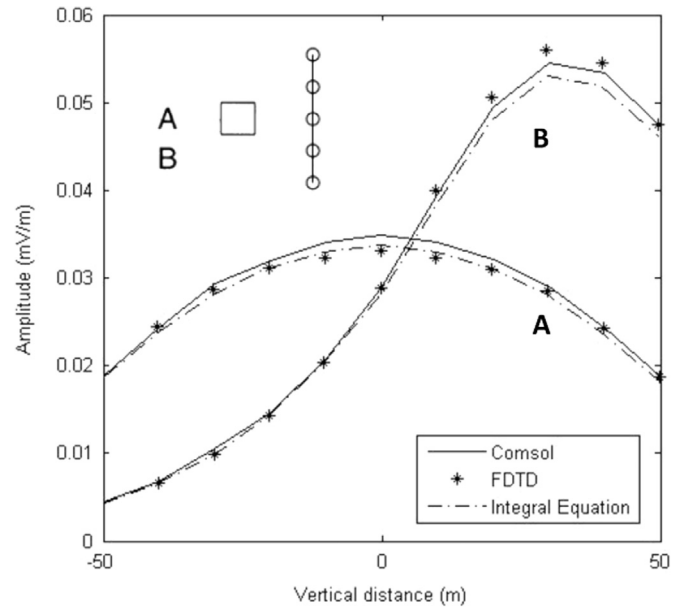

Fig. 5. Modeling results of a 0.1 S/m cubic model by Comsol Multiphysics (solid line), FDTD (asterisks) and integral equation method (dashed-dotted line). The data derived using FDTD method and integral equation method are from Yu et al. (1998). The geometry is shown as a cross section view in the top left of the figure and the five open circles represent the receiver locations (although there are more than 5).

transmitter spacing 20 m (so there are 18 transmitter locations in total). The transmitter frequency is 2.5 MHz and the dipole moment is 4000 Am. The receivers (RX) are along the line from (−200, 0, 100) to (−200, 0, 440). There are two targets in the model. Target 1 (T1) is a rectangular prism, with its center at (−110, 0, 175). Its cross section on the XZ-plane is a 96×32 m^2 rectangle, with a 45 degree dip; the strike length is 96 m in the y-direction, with its center at the XZ-plane. Target 2 (T2) is a 32 m-thick layer dipping at a 55.4 degree angle, starting at (−60, 0, 400), all the way to the left edge of the model near $x=-240$. Its strike length is 300 m, with its center at the XZ-plane. The rectangular prism bounded on the left and right by the TX and RX boreholes, with a strike length of 200 m, is the region of interest selected for finer discretization. The size of the whole model is $400\times400\times560$ m^3, including a 50 m-thick PML on the edge of the model (Fig. 6a).

The model has conductivities of 0.001 S/m for T1 and T2, and 0.0001 S/m elsewhere. Other physical parameters are $\varepsilon_r=6.5$ and $\mu_r=1$ for the whole model. The wavelength is 46.96 m in the background, and 42.14 m for T1 and T2. We discretize the model with element sizes of 3–5 m in T1 and T2, and 4–6 m elsewhere within the region of interest, giving cells that are approximately 1/8th of the wavelength. From the outer surface of the region of interest to the PMLs, the edge length of the element can increase to 20 m. By numerically solving Maxwell's equations, the x-, y-, and z-components of the electric field on the nodes of the elements will be determined. Along the receiver borehole, the node spacing is 4–6 m, but we can interpolate to get the z-component E field response every meter.

As one example we have plotted the z-component amplitude data for the case when the transmitter is at $z=280$ m (Fig. 6b). The dashed profile is the data in a homogeneous model with conductivity of 0.0001 S/m (and peaks at the same depth as the source −280 m), while the solid profile is the synthetic data with T1 and T2 inserted into the model. It can be seen from the figure that in the second case receiver data are attenuated by the presence of T1 and T2, with the profile peaking at $z=160$ m, where a ray from the
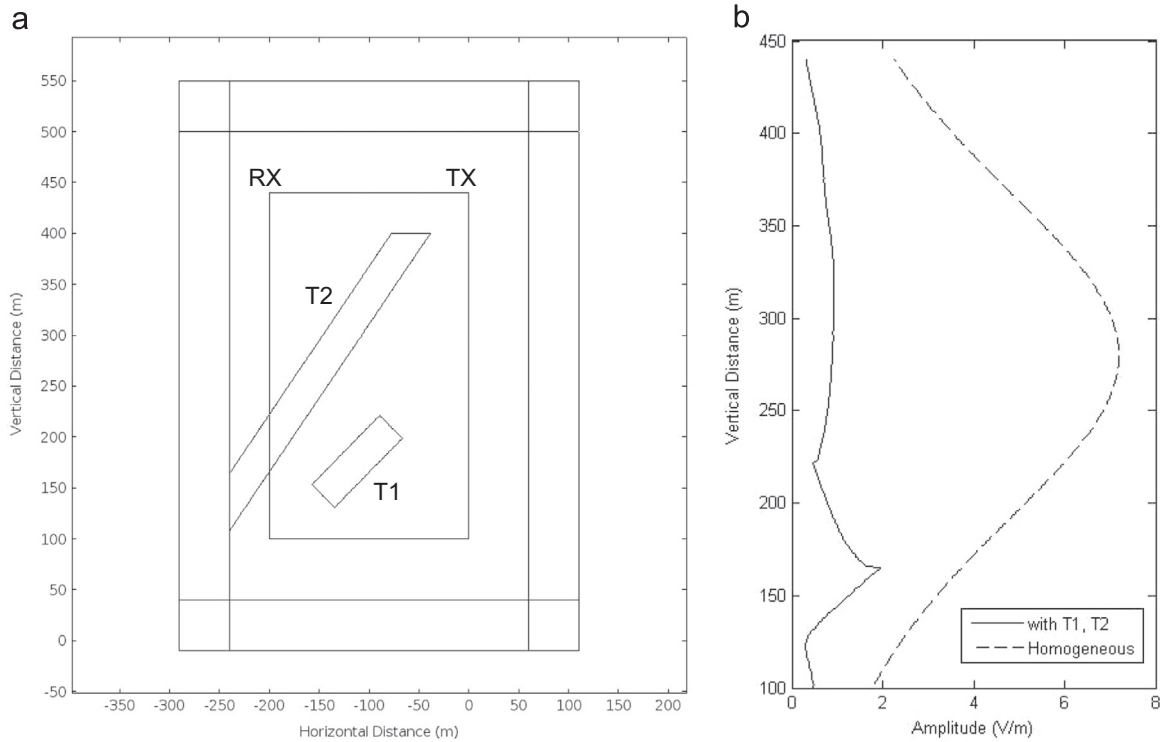
Fig. 6. (a) *XZ*-plane view of the synthetic model with two vertical boreholes containing the transmitter (right) and receiver (left). There are two anomalous bodies T1 and T2, centered on the *XZ* plane with strike lengths of 96 and 300 m respectively. The inner rectangle is the region of interest, and the PML is between the outer two rectangles. The strike length of the whole model is 400 m. (b) Receiver profiles of transmitter position at *z*=280 m with (solid) and without anomalies (dashed).

transmitter would pass through the gap between T1 and T2. The receiver data has its lowest value at *z*=220 m, which corresponds to the upper edge of the T2, where a ray from the transmitter has the longest passage through T2. The receiver profiles on Fig. 6b show that for this frequency, straight ray attenuation theory can generally represent the characteristics of the response.
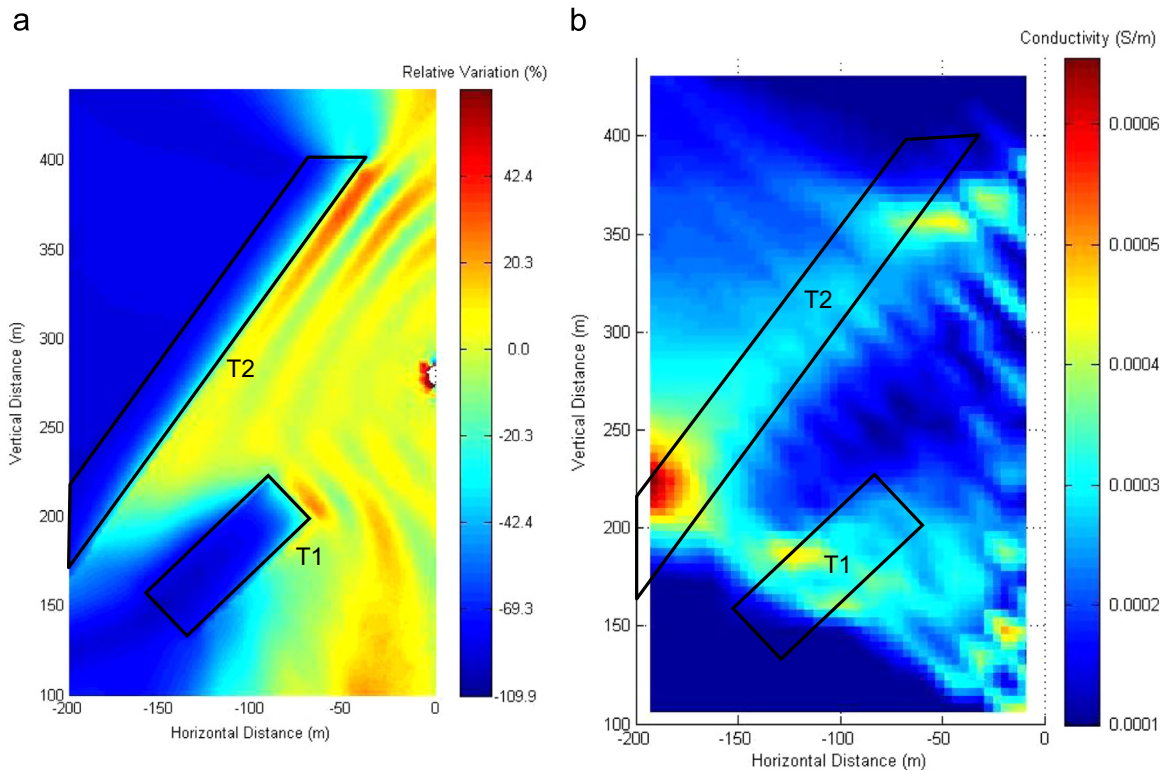

Fig. 7. (a) Relative variation map for the case when the transmitter is at *z*=280 m. (red is increased relative to the homogeneous whole space and blue is decreased) (b) Imaging results of SIRT algorithm. Outlines of T1 and T2 are added for comparison. (For interpretation of the references to color in this figure legend, the reader is referred to the web version of this article)

To study the spatial variation of the EM field on the XZ plane for the case when the transmitter is at $z=280$ m, we exported the z-component data from Comsol and calculated the relative variation on the plane. The relative variation is defined as the difference from the homogeneous model data at the corresponding position normalized by the homogeneous model data,

$$V_R = \frac{A_a - A_h}{A_h} \times 100\%, \tag{5}$$

where, V_R is the relative variation; A_a is the amplitude data with the anomalous models T1 and T2; and A_h is the homogeneous model amplitude data. From the map of the relative variation on the plane (Fig. 7a), we can see where and how much the field is increased or decreased by the T1 and T2. Warm colors represent an increase, while cool colors depict a decrease. The straight ray attenuation theory can explain the shadow zone within and behind T1 and T2, but does not work well near the edges of the conductive bodies. The shadow, created by T1, has a larger area than would be predicted by the straight-ray model. The attenuation is strong right behind the conductive bodies, and changes gradually to non-attenuated field, far away from the edges of the objects. There are striped patterns between the source and the conductive bodies, which cannot be interpreted with the straight-ray theory either. One possible explanation is the EM wave is reflected at the surface of the conductive bodies, and is shifted slightly in phase and interferes with source field causing the increased and decreased fields with a wavy pattern. Considering the wavelength of the background is 46.96 m the closest conductive anomaly is almost 100 m away from the source, which is about twice the wavelength. In this case, $|kr|=13.40$, which satisfies the condition that $|kr| \gg 1$, so the second order term, which is inductive contribution, is small. We infer that the induction phenomenon will only have a minor effect in this case.

To study the imaging methods, we export the receiver data for all the transmitter locations, and input the synthetic data into a tomographic algorithm. Here we give an example of the Simultaneous Iterative Reconstruction Technique (SIRT) algorithm (Jackson and Tweeton, 1994; Pears and Fullagar, 1998). The SIRT algorithm (based on the straight-ray EM propagation model), together with the data pre-processing, has been implemented in the ImageWin program (www.fullagargeophysics.com). Here, we process the data as follow: (1) converting the amplitude data to decibel units by taking the logarithm; (2) radiation pattern correction using an assumed spherical spreading; (3) source strength correction using the source term calculated with the transmitted current. The borehole plane is discretized with a pixel size of 4×4 m^2. The attenuation of a certain ray path is the sum of the attenuations in each pixel the ray passed through. The attenuation in each pixel is the product of the attenuation rate and the distance that the ray traverses in that specific pixel. The distance can be calculated according to the geometry of the borehole plane and the pixel size (assuming a straight ray). We can use these relations to construct a set of equations. By solving the equations, we reconstruct an image of attenuation rate on the borehole plane (Hill, 1984). After that, we transform the attenuation rate to conductivity by rearranging equation (1.49) in Ward and Hohmann (1988),

$$\alpha = \left\{ \frac{\omega^2 \mu \varepsilon}{2} \left[\left(1 + \frac{\sigma^2}{\varepsilon^2 \omega^2} \right)^{1/2} - 1 \right] \right\}^{1/2}, \tag{6}$$

where, α is the attenuation rate. Fig. 7b shows the transformed conductivity data.

We can see that the imaging results of the SIRT algorithm are of acceptable quality, with the locations and the shapes of T1 and T2

being somewhat blurred. There is a good ability to identify the middle of T1, but not the bottom. The location where T2 intersects the receiver line dominates the image. However, the length of T2 is only weakly resolved, and the top is displaced somewhat. The value of the background conductivity seems reasonably resolved, but the value of the conductivity in the conductive anomalous zones is not successfully recovered. There are some artifacts near the transmitted borehole. Some defects are inherent in the RIM method, which means that the imaging quality could not be improved with any imaging method; for example, the smeared area on the upper-left of the image is due to poor data coverage. We can see that the lower edge of the T2 is better resolved than the upper edge, because the lower edge is closer to the center of the cross-hole section, where more rays are coming from a larger angle range, which gives the lower edge a better data coverage (Jackson and Tweeton, 1994). However, some problems might be due to the ray-based imaging method, for example, a poor ability to distinguish T1 and T2. Fig. 7a shows that the EM-field propagation does not follow a precise straight ray path. Alternative imaging methods based on a curved-ray model or diffraction tomography (Devaney, 1984; Nekut, 1994), may possibly give better imaging results. However, based on the current observation, we cannot draw strong conclusion. We need to carry out further studies to find out what kinds of imaging methods are appropriate for the RIM data, and the Comsol package can play a role in generating synthetic RIM data where the electric properties are known.

5. Conclusions

The ability of the Comsol RF module to simulate RIM data was investigated. By comparing the Comsol modeling results (with 6 types of element sizes at 4 frequencies) with the analytical solution for the homogeneous whole space, we find that the synthetic data generated with 5 elements per wavelength have modeling errors less than 5%; 7–8 elements per wavelength yield the errors around 1%; and 10 elements per wavelength give errors less than 1%. The comparison studies for anomalous models show that the Comsol modeling results are consistent with the analytical solutions and the solutions of other numerical modeling methods. Further, the guidelines for element sizes derived from homogeneous whole space models can be applied to inhomogeneous models.

We provide a modeling example with two moderately conductive bodies between boreholes to illustrate the modeling capability of the Comsol package. In the example, we use a receiver profile and the relative variation map to understand the physical phenomena of radio-frequency EM waves. We find that attenuation in the two conductive bodies is apparent in the relative variation maps and that a shadow cast by the transmitter is also apparent; however, this shadow is not as sharp as the ray theory would predict. Some reflections are also apparent between the source and the conductive bodies. The imaging example reveals that with the SIRT algorithm, the location and the shape of the conductive anomalies can be reconstructed somewhat successfully. The imaging results have some problems such as low resolution, incorrect conductivity estimation, and some artifacts. To better understand the imaging algorithms, we need further studies, and the Comsol package can serve as a useful FEM modeling tool for these studies.

Reference

Bondeson A., Rylander T., Ingelström P., 2005. Computational Electromagnetics. Texts in Applied Mathematics. Springer New York, Vol. 51. doi: 10.1007/b136922.222pp.

Butler, S.L., Sinha, G., 2012. Forward modeling of applied geophysics methods using Comsol and comparison with analytical and laboratory analog models. Comput. Geosci. 42, 168–176. http://dx.doi.org/10.1016/j.cageo.2011.08.022.

Devaney, A.J., 1984. Geophysical diffraction tomography. IEEE Transac. Geosci. Remote Sens. GE-22 (1), 3–13. http://dx.doi.org/10.1109/TGRS.1984.350573.

Dines, K.A., Lytle, R.J., 1979. Computerized geophysical tomography. Proc. IEEE 67 (7), 1065–1073. http://dx.doi.org/10.1109/PROC.1979.11390.

Hill, D., 1984. Radio propagation in a coal seam and the inverse problem. J. Res. Natl. Bur. Stand. 89 (5), 385–394. http://dx.doi.org/10.6028/jres.089.022.

Holliger, K., Musil, M., Maurer, H.R., 2001. Ray-based amplitude tomography for crosshole georadar data: a numerical assessment. J. Appl. Geophys. 47 (3–4), 285–298. http://dx.doi.org/10.1016/S0926-9851(01)00072-6.

Jackson, M.J., Tweeton, D.R., 1994. MIGRATOM—Geophysical Tomography Using Wavefront Migration And Fuzzy Constraints. Department of Interior, US Bureau of Mines, Minneapolis, MN, USA, Report of Investigations RI9497.

Johnson, D.M., 1997. Finite difference time domain modeling of cross-hole electromagnetic survey data. University of Utah, Salt Lake City, UT, USA, M. Sc. Thesis.

Korpisalo, A., Heikkinen, E., 2014. Radiowave imaging research (RIM) for determining the electrical conductivity of the rock in borehole section OL-KR4-OL-KR10 at Olkiluoto, Finland. Explor. Geophys. . http://dx.doi.org/10.1071/EG13057

Monaghan, W.D., 2007. Experimental studies of electromagnetic signals to enhance radio imaging method (RIM). West Virginia University, Morgantown, WV, USA, M. Sc. Thesis.

COMSOL Multiphysics User Guide, 2012. Version 4.3 a, COMSOL AB, Stockholm, Sweden.

Mutton, A.J., 2000. The application of geophysics during evaluation of the century zinc deposit. Geophysics 65 (6), 1946–1960. http://dx.doi.org/10.1190/1.1444878.

Naprstek, T., 2014. Modelling Radio Imaging Method Data Using Electric Dipoles In A Homogenous Whole Space. Laurentian University, Sudbury, ON, Canada, M. Sc. Thesis.

Nekut, A.G., 1994. Electromagnetic ray-trace tomography. Geophysics 59 (3), 371–377. http://dx.doi.org/10.1190/1.1443599.

Park, J., Bjørnarå, T.I., Farrelly, B.A., 2010. Absorbing boundary domain for CSEM 3D modelling. In: Excerpt from the Proceedings of the COMSOL Conference 2010, Paris.

Pears, G.A., Fullagar, P.K., 1998. Weighted tomographic imaging of radio frequency data. Explor. Geophys. 29 (3–4), 554–559. http://dx.doi.org/10.1071/EG998554.

Thomson, S., Hinde, S., 1993. Bringing geophysics into the mine: radio attenuation imaging and mine geology. Explor. Geophys. 24 (3–4), 805–810. http://dx.doi.org/10.1071/EG993805.

Ward, S.H., Hohmann, G.W., 1998. Electromagnetic theory for geophysical applications. In: Nabighian, M.N. (Ed.), Electromagnetic Methods in Applied Geophysics Vol. 1. Society of Exploration Geophysicists, pp. 131–311. http://dx.doi.org/10.1190/1.9781560802631.ch4.

Wilkinson, P.B., 2005. Cross Borehole Electromagnetic Tomography: Scoping Study And Literature Review. British Geological Survey, Keyworth, Nottingham, England, Internal Report IR/05/146.

Xiong, Z., Tripp, A.C., 1997. 3-D electromagnetic modeling for near-surface targets using integral equations. Geophysics 62 (4), 1097–1106. http://dx.doi.org/10.1190/1.1444210.

Yu, L., Chouteau, M., Boerner, D.E., 1998. On the imaging of radio-frequency electromagnetic data forcross-borehole mineral exploration. Geophys. J. Int. 135 (2), 523–541. http://dx.doi.org/10.1046/j.1365-246X.1998.00655.x.

Zhou, B., Fullagar, P.K., Fallon, G.N., 1998. Radio frequency tomography trial at Mt Isa Mine. Explor. Geophys. 29 (3–4), 675–679. http://dx.doi.org/10.1071/EG998675.